International Journal of Technology 11(2) 310-321 (2020)
Received March 2019 / Revised October 2019 / Accepted March 2020

International Journal of Technology

http://ijtech.eng.ui.ac.id

Physical and Microwave Absorption Characteristics of High Powered Ultrasonically Irradiated Crystalline $BaFe_9Mn_{1.5}Ti_{1.5}O_{19}$ Particles

Erlina Yustanti[1*], Adhitya Trenggono[1], Azwar Manaf[2]

[1]*Department of Metallurgical Engineering, Faculty of Engineering, Sultan Ageng Tirtayasa University, Jl. Jenderal Sudirman KM 03 Cilegon, Banten 42435, Indonesia*
[2]*Department of Physics, Faculty of Mathematics and Natural Science, Universitas Indonesia, Kampus UI Depok, Depok 16424, Indonesia*

Abstract. Barium hexaferrite (BHF) with the chemical formula $BaFe_{12}O_{19}$ is a well-known permanent magnet and is still primarily used in various electrical devices. Because of its excellent magnetic properties, BHF is potentially one of the best candidates as a microwave absorber. For this investigation, the magnetic and microwave absorption characteristics of nanostructured BHF and $BaFe_9Mn_{1.5}Ti_{1.5}O_{19}$ were study. The high coercivity of BHF was substantially reduced through Mn-Ti partial substitution for Fe atoms with a minor reduction of its saturation magnetization. Nanostructured Mn-Ti–doped BHF was obtained through particle size reduction with high-powered ultrasonic irradiation. After 12 h of ultrasonic irradiation, the mean particle of BHF reduced to 61 nm from 380 nm, and the Mn-Ti–doped BHF reduced from 545 nm to 95 nm. The mean crystallite size of the two samples was 15 and 18 nm, respectively. Hence, the particles of both samples contained only a few crystallites. The characterization of reflection loss revealed that the highest absorption value achieved by the nanostructured $BaFe_9Mn_{1.5}Ti_{1.5}O_{19}$ sample was 19.75 dB at 13.6 GHz, and approximately 90% of the intensity of incoming electromagnetic waves was reduced by the material.

Keywords: Barium hexaferrite; Mechanical alloying; Reflection loss; Ultrasonic irradiation

1. Introduction

Barium hexaferrite (BHF) is a permanent magnetic material characterized by high values of coercivity, saturation magnetization, magnetic transition temperature, and corrosion resistance (Kerschl et al., 2002). The high value of saturation magnetization in BHF provides an opportunity for employing it in microwave absorption applications. However, its high coercivity must be reduced to some extent to facilitate the interaction between the magnetic field of electromagnetic waves and the magnetization of BHF. The reduced coercivity of Mn-Ti–substituted BHF was shown to increase microwave absorption (Manaf et al., 2017). Studies have shown that $BaFe_{12-y}Mn_yTi_yO_{19}$ (y = 0.0; 0.5; 1.0; 1.5) with y = 1.5 was the best absorption up to a 40 dB reflection loss in 1–5 GHz (Priyono and Manaf, 2009). BHF as an electromagnetic wave absorber is widely used in many applications like information, communication using electronics components, and radar-absorbing material (Priyono and Manaf, 2009; Adi et al., 2017; Fitriana et al., 2017; Manaf et al., 2017).

*Corresponding author's email: erlina.yustanti@untirta.ac.id, Tel.: +62-254-395502
doi: 10.14716/ijtech.v11i2.2988

Mechanical alloying is a simple tool for the preparation of crystalline materials. Mn-Ti–substituted BHF has been employed by several researchers to prepare microwave absorption materials. Large crystallites resulting from mechanical alloying can be further fragmented to smaller sizes of crystallites by means of high-powered ultrasonic irradiation. There have been several methods available for the fabrication of nanoparticles, including salt-assisted ultrasonic spray pyrolysis (Hwan An et al., 2014), microwave-induced combustion (Fu et al., 2003), ceramic routing (Hessien et al., 2007), microwave-hydrothermal (Sadhana et al., 2012), and citrate sol–gel combustion routing (Sözeri et al., 2012). Mechanical alloying has some advantages: it is a simple technique, produces waste-free material, and can be implemented on a large scale.

In terms of magnetic properties, remanence and coercivity are affected by crystallite size. Magnetic materials with nanostructures allow the grain exchange interaction effect, resulting in enhanced remanence and reduced coercivity (Manaf et al., 1993). The effect is further beneficial for microwave absorption applications since nanoscale crystallites have become a center for electromagnetic wave scattering due to a high density of surfaces in the material. A combination of high remanence and nanostructure would be a potentially powerful source for electromagnetic wave absorption.

In this work, we explored the potential of BHF and its physical effects on its magnetic properties and microwave absorption characteristics. BHF-based magnetic materials were fabricated through mechanical alloying combined with high-powered ultrasonic irradiation. The material under study is $BaFe_9Mn_{1.5}Ti_{1.5}O_{19}$, a selected composition from the $BaFe_{12-y}Mn_yTi_yO_{19}$ (y = 0.0, 0.5, 1.0, and 1.5) series, which has been previously studied (Priyono and Manaf, 2009; Repi and Manaf, 2012; Manawan et al., 2014). However, the focus of the current work of this composition is to further explore its excellent absorption characteristics.

2. Experimental Methods

Stoichiometry quantities of standard research-grade $BaCO_3$, Fe_2O_3, $MnCO_3$, and TiO_2 precursors of Sigma-Aldrich with at least 99% purity level were mixed and milled in a planetary ball mill apparatus for preparation of BHF and $BaFe_9Mn_{1.5}Ti_{1.5}O_{19}$ (BFMTO). The mass ratio between precursors and balls mill was 1:10. All mixed precursors were mechanically milled at 160 rpm for 60 h and produced heavily deformed powder materials. The paste was then dried in an oven to release the water content and packed together in a cylindrical die at a 10-ton load. It produced green compact samples that were 25 mm in diameter and 3 mm thick. The green compact samples were sintered at 1100°C for 4 h, leading to polycrystalline samples. Ultrasonic irradiation was then employed on the polycrystalline powder of each sample obtained after being remilled for 20 h. The powder was further refined using the Qsonica Sonicator Q700 (20 kHz and 60 µm amplitude) for up to 12 h. The ultrasonic irradiation was applied to the dispersed media containing particles with concentrations of 10, 30, and 50 g/L to produce monodispersed particles. The addition of 0.54 µL non-ionic polyoxyethylene 20 sorbitan monolaurate of 0.01 as a surfactant was required to prevent agglomeration before the completion of the ultrasonic irradiation.

All mechanically alloyed samples were evaluated using an XRD PANalytical Empyrean with an X'Pert MPD diffractometer (Cu Kα radiation, λ = 1.5406 Å, and generator settings of 30 mA and 40 kV). The ultrasonically irradiated particles were evaluated using XRD for quantitative analysis by the whole powder pattern modeling (WPPM) software to obtain crystallite size distribution. The magnetic properties were evaluated using a hysteresis graph (PERMAGRAPH® L MAGNET-PHYSIK Dr. Steingroever GmbH), and microwave characteristics were evaluated using a KEYSIGHT PNA-L Network Analyzer N5232A in the frequency range of 8–20 GHz. Sample BHF and BFMTO were placed in a sample holder of VNA with a dimension of height 10.15 mm, width 22.85 mm, and thickness 1.8 mm. We

calculated reflection loss (RL) using the Nicolson–Ross–Weir method (Nicolson and Ross, 1970) from the measurement of the transmitted signal (S21) and reflected signal (S11) using Equations 1 and 2.

$$RL\ (dB) = 20 \log [(Z - 1)/(Z+1)] \quad (1)$$

$$Z = \sqrt{\mu/\varepsilon}\ \tanh [(-j2\pi f d/c)\sqrt{\mu.\varepsilon}] \quad (2)$$

where Z is the characteristic impedance of samples, μ is complex relative permeability ($\mu = \mu' - j\mu''$), ε is complex relative permittivity ($\varepsilon = \varepsilon' - j\varepsilon''$), f is the frequency of the electromagnetic wave, d is the thickness of the samples, and c is the light velocity. The distribution of particle sizes was obtained with the particle size analyzer (PSA) Malvern Zetasizer Nano ZS. The transmission electron microscope (TEM) FEI Tecnai G2 SuperTwin was employed in the microstructure studies.

3. Results and Discussion

3.1. Structural and Physical Characterization

The X-ray diffraction patterns obtained from the XRD examination of $BaO.6Fe_{2-x}Mn_{x/2}Ti_{x/2}O_3$ samples with $x = 0$ and 0.5 are displayed in Figures 1a and 1b, respectively, along with a fitting curve on each diffraction trace. Obviously, the diffraction peaks are mostly broadening (see the inset), suggesting that the crystallites in the samples were of ultra-fine size. Diffraction data of each pattern were further analyzed by software based on WPPM (Scardi and Leoni, 2002; Leoni et al., 2006) to determine the crystallite size.

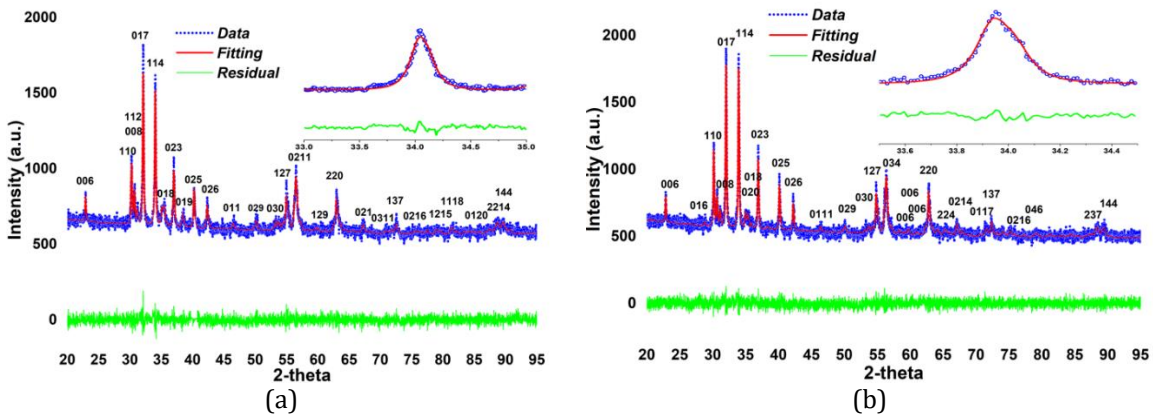

Figure 1 Diffraction pattern of $BaO.6Fe_{2-x}Mn_{x/2}Ti_{x/2}O_3$ (a) x = 0; and (b) x = 0.5

Table 1 Results of XRD data refinement studies for $BaO.6Fe_{2-x}Mn_{x/2}Ti_{x/2}O_3$ (x = 0 and 0.5) samples

Description	x = 0	x = 0.5
Goodness of Fit	1.09	1.08
Chemical Formula	$BaFe_{12}O_{19}$	$BaFe_9Mn_{1.5}Ti_{1.5}O_{19}$
Calculated Density (g/cm³)	5.30	5.26
Crystal Structure	Hexagonal	Hexagonal
Lattice Parameters (Å)		
a = b	5.889	5.904
c	23.187	23.236
α, β, γ (deg.)	90, 90, 120	90, 90, 120
Volume of Cell/10^{-3} Nm³	696.53	701.50

Table 1 summarizes the results of the XRD refined data analysis of two samples for comparative study. For both patterns, theoretical and experimental data are well fitted; these are indicated by flat residue data within the scanned 2-theta diffraction angle. The formation of a single phase at the peak of the diffraction pattern was well confirmed, according to international crystal structure database number 98-006-0985, in which the two diffraction traces correspond to the $BaFe_{12}O_{19}$ phase. The calculated mass density of sample x = 0.5 was slightly lower than that of x = 0 because of the increase in the cell unit volume.

The goodness of fit for the two traces was almost identical, with a value near 1.0, indicating that the refined data should result in reliable information. It was then confirmed that the two samples were a single-phase material with hexagonal $BaFe_{12}O_{19}$ as the only phase present in the samples. Figure 2 shows a small change occurring due to the Mn-Ti substitution. The diffraction pattern shift is generally due to crystal defects, including substitution or surface roughness and the non-alignment of samples during the experiment.

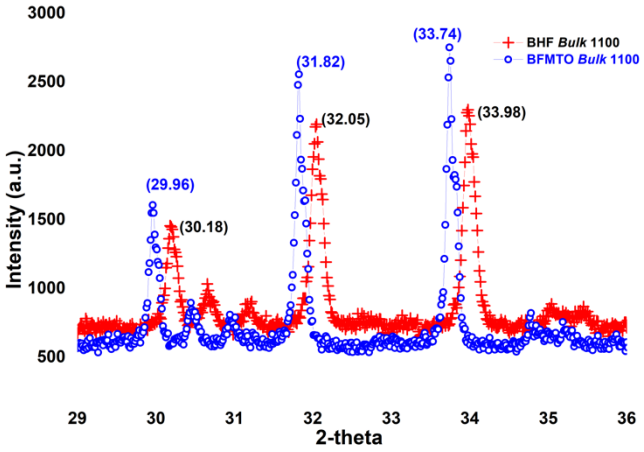

Figure 2 Shifting of XRD diffraction peaks due to Mn-Ti substitution

Physical characterization of the mechanically alloyed BHF and BFMTO samples are shown in Table 2. The milling process yielded a mean particle size of 2.1 μm and 1.9 μm for BHF and BFMTO samples, respectively. Milling involved the mixing of precursors to form paste through the milling process for 60 h followed by sintering at 1100°C for 4 h to become polycrystalline bulk samples. The powdered material from the milling process consisted of multi-crystallite particles with mean crystallite sizes of 110 nm and 279 nm, respectively. Hand grinding involved manual grinding and sieving for bulk samples with a width of 2.5 cm and a thickness of 3 mm until a powder was obtained. Hand grinding obtains a more even powder size by using 60-mesh sieving. Hand grinding the powdered material of the two samples helped reduce the particle size down to 1.1 μm and 0.9 μm, respectively, but the mean crystallite size remained unchanged. Hand grinding was shown to be previously effective in reducing particle sizes (Yustanti et al., 2016). However, this is only practicable for a small portion of the materials. The most efficient manner to further bring down the sizes of crystallites in mechanically alloyed powder is to precede the remilling treatment of the crystalline powder with a long milling period. Remilling involved milling again to smoothing the particle size for 20 h to prepare irradiated sonication process effectively when the particle size was at least 600 nm. Such particle and crystallite sizes suggest that the milled particles still contained multi-crystallite particles. We then introduced an additional treatment to transforms the multi-crystallite particle to monocrystallite particles through high-powered ultrasonic irradiation treatmen.

The particle size distribution of the BHF and BFMTO obtained after ultrasonic irradiation that was applied to the particles in dispersed media of three different concentrations is shown in Figure 3. Even after 3 h of irradiation, the mean particle size was still between 260 nm (BHF) and 355 nm (BFMTO). The particle concentration in a dispersion medium determines the mean size value of the particles under ultrasonic irradiation. The ultrasonic irradiation was effective when applied to the particles in dispersed media of low density. When the particle density in the ultrasonic reactor is relatively high, even though the bubble burst produces ultrasonic waves with high pressure, particles can only accelerate at low particle speeds. Impact energy may not be large enough to break down the particles (Ali et al., 2014).

Table 2 Reduction of BHF and BFMTO particle and crystallite size in various processes

Process	Particle Size (nm)		Crystallite Size (nm)	
	BHF	BFMTO	BHF	BFMTO
Milling	2100	1900	110	279
Manual Grinding	1100	900	100	258
Remilling	380	545	39	39

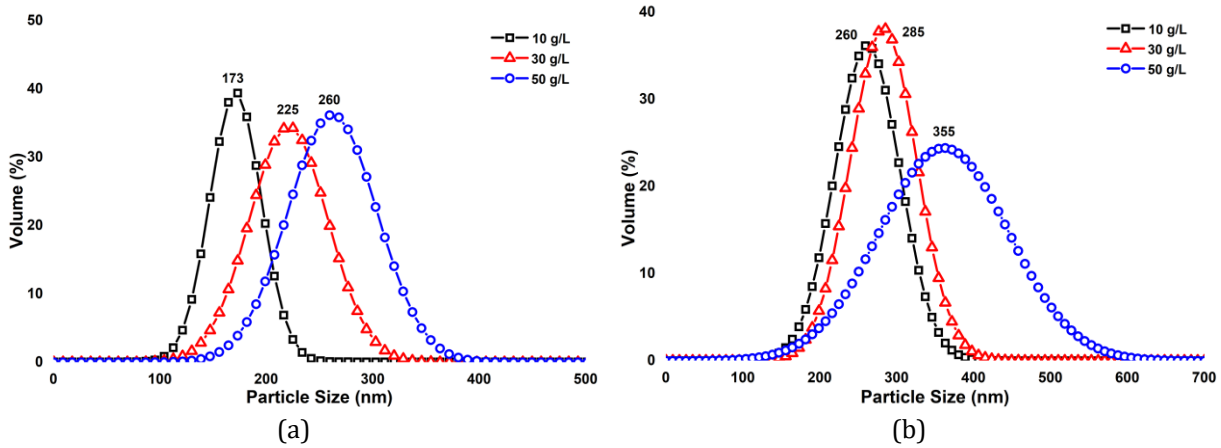

Figure 3 The particle size distribution after ultrasonic irradiation for 3 h: (a) BHF; and (b) BFMTO

Figure 4 shows the plots of particle size distribution of the two sample types, which show progressive size reduction after the ultrasonic irradiation at various irradiation times. Initially, the BHF particles had a mean size of 380 nm with a broadened size distribution where the sizes were in the range of 100–700 nm. Longer irradiation time resulted in finer particle size along with a progressive reduction in the size variation. Plots in Figure 4 demonstrate how the volume fraction of particles increased continuously with the increase in irradiation time. After 12 h of irradiation, the mean sizes of BHF and BFMTO particles were 61 nm and 95 nm, respectively.

The crystallite size of particles in dispersed media is less affected by ultrasonic irradiation according to the results of previous studies (Yustanti and Manaf, 2018; Yustanti et al., 2017), which also demonstrated that particle size tends to decrease significantly. High nucleation rates and large bubble sizes can be achieved when particle density in the reactor is low. The current finding confirms that the reduction of the particle density at 10 g/L was better than the values of 30 g/L and 50 g/L.

Table 3 shows that the mean particle sizes of BHF and BFMTO before treatment were 380 nm and 545 nm, respectively, and that they were brought down to 61 nm and 95 nm, respectively, after ultrasonic irradiation for 12 h. Hence, ultrasonic irradiation applied to the untreated particles reduced the particle size of the two samples by approximately six times than their initial size. However, the crystallite size only reduced to approximately half of the initial size after 12 h of irradiation.

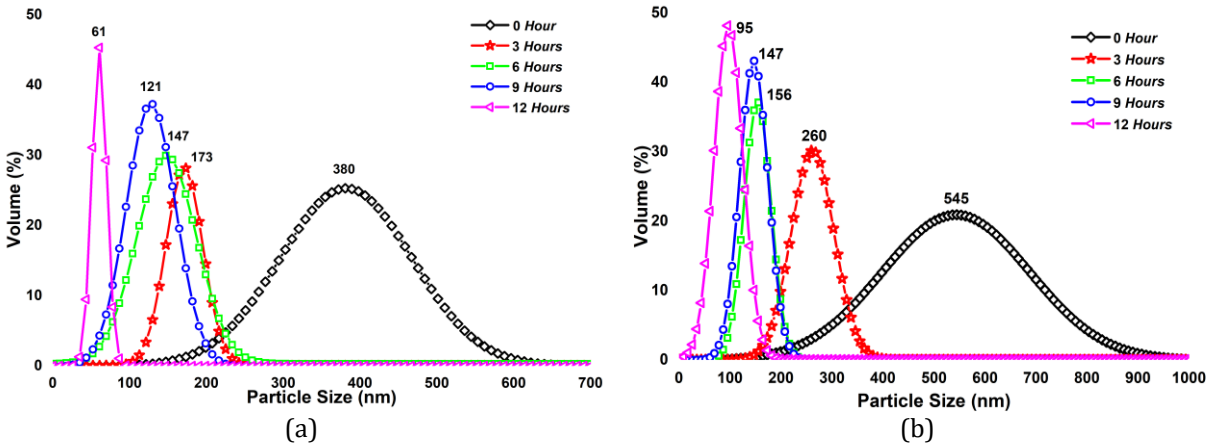

Figure 4 Effect of ultrasonic time on the reduction of particle size: (a) BHF; and (b) BFMTO

Table 3 Summary of the number of crystallites in the polycrystalline particles after being irradiated

Irradiation time (h)	BHF			BFMTO		
	Mean particle size (nm)	Mean crystallite size (nm)	N	Mean particle size (nm)	Mean crystallite size (nm)	N
0	380	39	925	545	39	2729
3	173	17	1054	260	22	1651
6	147	17	647	156	22	357
9	121	16	433	147	20	397
12	61	15	67	95	18	147

The number of crystallites in a particle (N) was calculated based on the assumption that the particle and crystallite are considered as a solid sphere. Data in Table 3 reinforce that the 12 h of ultrasonic treatment to the BHF and BFMTO particles was able to reduce the particles to the size of monocrystallite particles. Physical characterization of the particles subjected to ultrasonic irradiation demonstrates that ultrasonic irradiation is a reliable method of fabricating the monocrystallite particle with the size in the nanometer scale. The input energy of the instrument during irradiation is converted into heat in liquid media and wave energy on the transducer (Merouani et al., 2014). The irradiation power increases the wave energy in a liquid medium, when increased ultrasonic irradiation time and amplitude (Merouani et al., 2014). However, in this case, the increase in the particle density of liquid media provides non-optimal cavitation bubble formation, which is in line with the results of Ali et al. (2014). The size and number of cavitation bubbles formed and the lifetime of ultrasonic waves, which are strongly affected by power, frequency, and particle density in the ultrasonic reactor (Kanthale et al., 2008), all determine the effectiveness of the refinement of the particles. Particle and crystallite sizes determined by PSA and XRD,

respectively. Figure 5 shows a comparison micrograph of SEM and TEM in the BMFTO sample. Figure 5a shows that the mean particle size of BFMTO before ultrasonic irradiation was 585 nm. However, after 12 h of ultrasonic irradiation, the average particle size of BFMTO decreased dramatically to 28 nm (Figure 5b). Analysis of particle size distribution on SEM and TEM was conducted using imageJ software.

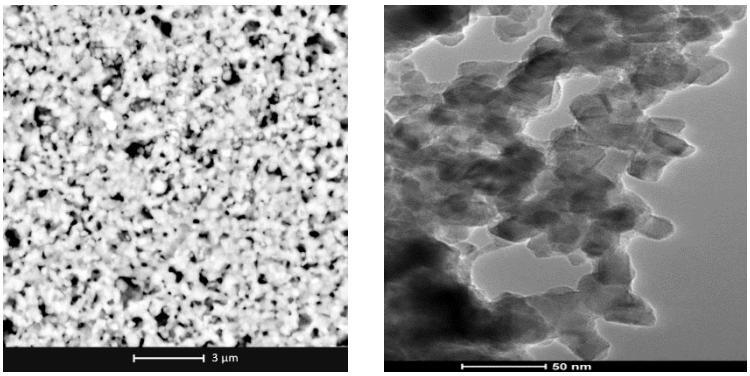

(a) (b)

Figure 5 Micrograph of particles size of BFMTO: (a) SEM-FEI before ultrasonic irradiation; (b) TEM after 12 h of ultrasonic irradiation

3.2. Magnetic and Microwave Absorption Characteristics

Figure 6a shows a comparison of the hysteresis loop of two BHF samples before and after additional ultrasonic irradiation with that of BFMTO. The two BHF samples differed only in their respective mean particle sizes. Their remanence and coercivity before receiving ultrasonic irradiation were 0.20 T and 248 kA/m, respectively, whereas the remanence and coercivity of the ultrasonically treated samples were 0.23 T and 203 kA/m, respectively. Hence, the treated sample had a remanence enhancement and a slightly reduced coercivity, a typical effect of grain exchange interaction (Hadjipanayis and Prinz, 1991). According to the data in Table 3, the mean crystallite size of BHF samples before and after ultrasonic irradiation were 39 nm and 15 nm, respectively. These values are far below the size of a single domain particle (460 nm) for the BHF (Rezlescu et al., 1999). Hence, enhancement in remanence and reduced coercivity occurred only in a BHF sample with an average crystallite size of 15 nm. The total surface-to-volume ratio of crystallites in the sample was likely the reason for the remanence enhancement. The finer the crystallite size, the higher the surface-to-volume ratio of the sample.

Based on the random orientation model (isotropic) of non-interacting particles, remanence to the saturation magnetization ratio J_r/J_s should have been ≤ 0.5 (Stoner and Wohlfarth, 1948). If J_s = 0.39 T (Liu et al., 2006) is taken as a reference for the calculation of the J_r/J_s ratio, the calculated J_r/J_s values of 0.51 and 0.59 are obtained from the BHF samples before and after ultrasonic treatment, respectively. The higher J_r value of the treated sample than the untreated one is evidence of the inter-grain exchange interaction effect on the nanoparticle system (Hadjipanayis and Prinz, 1991). In addition to this, a slight reduction of the corresponding coercivity in the treated sample provided further evidence of the effects (Herzer, 2005). The reduced coercivity is associated with average out the anisotropy constant of individual crystal within the exchange-coupled volume as addressed by Herzer in the so-called random anisotropy model (Herzer, 1989; Herzer, 1990). According to the model, the average anisotropy constant of the magnetic phase is reduced by the exchange length $L_{ex.}$ (Herzer, 2005). The calculated L_{ex} value of the BHF is 31 nm subject to J_s = 0.39 T value and the *exchange stiffness constant*, A = 10^{-11} J/m (Herzer, 1990). L_{ex} is twice the mean

crystallite size of the ultrasonically treated BHF sample (15 nm, see Table 3). Hence, remanence enhancement and reduced coercivity obtained in the ultrasonically treated sample suggests that inter-grain exchange interaction took place in the sample. Nevertheless, grain exchange interaction has little effect on the remanence enhancement in the BHF sample that received no ultrasonic treatment.

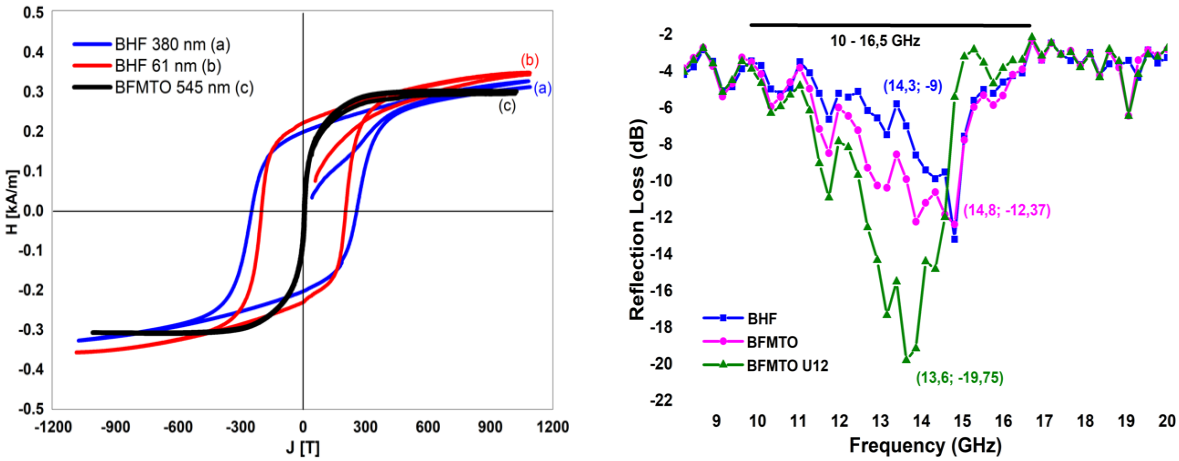

(a) (b)

Figure 6 (a) Loop hysteresis and (b) RL value of BHF, BFMTO, and BFMTOU12 in the frequency range of 8–20 GHz

Figure 6b shows comparisons of plots of RL values of BHF, BFMTO, and BFMTOU12. A sample that coded BFMTOU12 refers to a sample of BMFTO after being ultrasonically treated for 12 h. All three samples showed their ability to absorb EM waves in the frequency range of 8–20 GHz when entering the material. Broadband and high percent absorption ability are one of the requirements of electromagnetic absorption (Zhao et al., 2015e). The BHF had an RL value of 9 dB at a frequency of 14.3 GHz, meaning that approximately 65% of the incoming EM intensity was absorbed by the BHF at that frequency. A slight increase in the RL value was obtained from the BFMTO, which showed approximately 75% absorption. The high value of RL was achieved in a BFMTO U12 sample, which revealed an absorption level of 19.75 dB at a frequency of 13.6 GHz in bandwidth between 11 and 15 GHz. Hence, almost 90% of the incoming EM wave intensity was absorbed by the material. EM wave absorption materials with excellent design and absorption potential such as high efficiency, absorption width, and small thickness are always interesting to be developed, which has been explored (Zhao et al., 2015a; Zhao et al., 2015b; Zhao et al., 2015e). The difference in the three samples was due to their microstructure in which the crystallite size determined the absorption enhancement, which was associated with larger amounts of wave-scattering sources in the nanocrystal system.

The amount of power absorbed by the material per unit volume (W/m^3) is determined by magnetic permeability (μ) and electric permittivity (ε). The imaginary part of the two quantities determines the quantities of magnetic and dielectric loss tangents, which represent the amount of the power losses of EM in the material. The higher the value of the loss tangent, the greater the power of EM loss in the materials. The loss of power through such a damping mechanism depends on the microstructure of the material. The amorphous crystallite surface acts as the wave-scattering source, which would reflect the EM wave in many directions (Zhao et al., 2017). Hence, extrinsically, the mean crystallite size in the nano-regime would be credited with the ability of the EM wave to absorb the materials. As shown by studies from previous researchers (Zhao et al., 2015c; Zhao et al., 2015d),

nanoparticles can be obtained through a bottom-up process by evaluating the particle size of the material. However, in this study, the production of nanoparticles was carried out with the aid of additional treatment by ultrasonic irradiation as schematically illustrated in Figure 7, the process of nanoparticle synthesis through two combined processes: mechanical milling and ultrasonic irradiation.

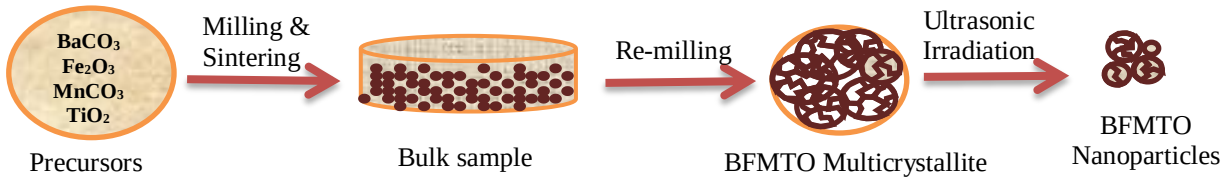

Figure 7 Schematic illustration of nanoparticle synthesis through mechanical milling and ultrasonic irradiation

As indicated in Figure 6b, the effect of nanoparticles obtained after 12 h of ultrasonic irradiation gave the best RL value of all samples analyzed. Nanoparticles in large numbers become an effective source of microwave scattering when the microwave enters the surface of particles in the material (Qiu et al., 2005). The result is that the absorption ability is enhanced, which is characterized by a large RL value.

4. Conclusions

Ultrasonic irradiation treatment to the mechanically alloyed BHF and BFMTO powders for 12 h resulted in monocrystalline powders with mean sizes of 15 and 18 nm, respectively. The BHF sample with a mean crystallite size of 15 nm allowed inter-grain exchange interaction, leading to a remanence-to-saturation ratio value of greater than 0.5. The BFMTOU12 sample with the mean crystallite size of 18 nm was characterized by a high RL value, where almost 90% of the incoming EM wave intensity was absorbed by the material.

Acknowledgements

Research work was funded by Sultan Ageng Tirtayasa University. The authors are grateful to the support of the Physics Department, Universitas Indonesia, for the research facilities.

References

Adi, W.A., Manaf, A., Ridwan, 2017. Absorption Characteristics of the Electromagnetic Wave and Magnetic Properties of the $La_{0.8}Ba_{0.2}Fe_xMn_{½(1-x)}Ti_{½(1-x)}O_3$ (x = 0.1–0.8) Perovskite System. *International Journal of Technology*, Volume 8(5), pp. 887–897

Ali, F., Reinert, L., Levêque, J.M., Duclaux, L., Muller, F., Saeed, S., Shah, S.S., 2014. Effect of Sonication Conditions: Solvent, Time, Temperature and Reactor type on the Preparation of Micron Sized Vermiculite Particles. *Ultrasonics Sonochemistry*, Volume 21(3), pp. 1002–1009

Fitriana, K.N., Hafizah, M.A.E., Manaf, A., 2017. Synthesis and Magnetic Characterization of Mn-Ti Substituted $SrO.6Fe_{2-x}Mn_{x/2}Ti_{x/2}O_3$ (x = 0.0–1.0) Nanoparticles by Combined Destruction Process. *International Journal of Technology*, Volume 8(4), pp. 644–650

Fu, Y.-P., Lin, C.-H., Pan, K.-Y., 2003. Fe/Ba Ratio Effect on Magnetic Properties of Barium Ferrite Powders Prepared by Microwave-Induced Combustion. *Japanese Journal of Applied Physics*, Volume 42(1,5A), pp. 2681–2684

Hadjipanayis, G., Prinz, G., 1991. Science and Technology of Nanostructured Magnetic Materials. In: *G. Hadjipanayis & G. Prinz, eds. NATO ASI Series, Series B: Physics, Advanced Science Institutes Series.* New York: PLenum Press, NATO Scientific Affairs Division

Herzer, G., 1989. Grain Structure and Magnetism of Nanocrystalline Ferromagnets. *IEEE Transactions on Magnetics*, Volume 25(5), pp. 3327–3329

Herzer, G., 1990. Grain Size Dependence of Coercivity and Permeability. *IEEE Transactions of Magnetics*, Volume 26(5), pp. 1397–1402

Herzer, G., 2005. The Random Anisotropy Model A Critical Review and Update. *In:* NATO Science Series II: Mathematics, Physics and Chemistry: Properties and Applications of Nanocrystalline Alloys from Amorphous Precursors (Pro size 2003), Volume 184, pp. 1–22

Hessien, M.M., Radwan, M., Rashad, M.M., 2007. Enhancement of Magnetic Properties for the Barium Hexaferrite Prepared through Ceramic Route. *Journal of Analytical and Applied Pyrolysis*, Volume 78(2), pp. 282–287

Hwan An, G., Yeon Hwang, T., Kim, J., Kim, J., Kang, N., Kim, S., Min Choi, Y., Ho Choa, Y., 2014. Barium Hexaferrite Nanoparticles with High Magnetic Properties by Salt-assisted Ultrasonic Spray Pyrolysis. *Journal of Alloys and Compounds*, Volume 583, pp. 145–150

Kanthale, P., Ashokkumar, M., Grieser, F., 2008. Sonoluminescence, Sonochemistry (H_2O_2 yield) and Bubble Dynamics: Frequency and Power Effects. *Ultrasonics Sonochemistry*, Volume 15(2), 143–150

Kerschl, P., Grössinger, R., Kussbach, C., Sato-Turtelli, R., Müller, K.H., Schultz, L., 2002. Magnetic Properties of Nanocrystalline Barium Ferrite at High Temperatures. *Journal of Magnetism and Magnetic Materials*, Volume 242-245(2), pp. 1468–1470

Leoni, M., Confente, T., Scardi, P., 2006. PM2K: *A flexible Program Implementing Whole Powder Pattern Modelling*. Zeitschrift fur Kristallographie, Supplement. Volume 23(23), pp. 249–254

Liu, Y., Sellmyer, D. J., Shindo, D., 2006. *Handbook of Advance Magnetic Material Volume 1: Nanostructural effects.* New York: Springer

Manaf, A., Buckley, R.A., Davies, H.A., 1993. New Nanocrystalline High Remanence Fe-Nd-B Alloys by Rapid Solidification. *Journal Magnetism and Magnetic Materials*, Volume 128(3), pp. 302–306

Manaf, A., Hafizah, M.A.E., Nainggolan, B.B., Manawan, M.T.E., 2017. Magnetic and Microwave Absorption Characteristics of Ti^{2+}- Mn^{4+} Substituted Barium Hexaferrite. *International Jornal of Technology*, Volume 8(3), pp. 458–465

Manawan, M., Manaf, A., Soegijono, B, Yudi, A., 2014. Microstructural and Magnetic Properties of Ti^{2+}-Mn^{4+} Substituted Barium Hexaferrite. *Advanced Materials Sciences and Technology*, Volume 896, pp. 401–405

Merouani, S., Hamdaoui, O., Rezgui, Y., Guemini, M., 2014. Energy Analysis during Acoustic Bubble Oscillations: Relationship between Bubble Energy and Sonochemical Parameters. *Ultrasonics*, Volume 54(1), pp. 227–232

Nicolson, M.A., Ross, G., 1970. Measurement of the Intrinsic Properties of Materials by Time-Domain Techniques. *IEEE Transactions on Instrumentation and Measurement*, Volume 19(4), pp. 377–382

Priyono, Manaf, A., 2009. Magnetic and Absorption Characteristics of Mn and Ti Substituted Barium Hexaferrite for Microwave Absorber. *In:* ICICI-BME 2009 Proceedings, pp. 160–163

Qiu, J., Shen, H., Gu, M., 2005. Microwave Absorption of Nanosized Barium Ferrite Particles Prepared using High-energy Ball Milling. *Powder Technology*, Volume 154(2-3), pp. 116–119

Repi, V.V.R., Manaf, A., 2012. Substitution Effect of (Mn, Ti) to the Dielectric Properties of Barium-Strontium Hexaferrite for Absorbing Electromagnetic Waves. *In*: International Conference on Physics and Its Applications, American Institute of Physics, Volume 1454(1), pp. 282–285

Rezlescu, L., Rezlescu, E., Popa, P.D., Rezlescu, N., 1999. Fine Barium Hexaferrite Powder Prepared by the Crystallisation of Glass. *Journal of Magnetism and Magnetic Materials*, Volume 193(1-3), pp. 288–290

Sadhana, K., Praveena, K., Matteppanavar, S. Angadi, B., 2012. Structural and Magnetic Properties of Nanocrystalline $BaFe_{12}O_{19}$ Synthesized by Microwave-Hydrothermal Method. *Applied Nanoscience*, Volume 2(3), pp. 247–252

Scardi, P., Leoni, M., 2002. Whole Powder Pattern Modelling. *Acta Crystallographica Section A: Foundations of Crystallography*, Volume 58(2), pp. 190–200

Sözeri, H., Durmuş, Z., Baykal, A. Uysal, E., 2012. Preparation of High Quality, Single Domain $BaFe_{12}O_{19}$ Particles by the Citrate Sol-Gel Combustion Route with an Initial Fe/Ba Molar Ratio of 4. *Materials Science and Engineering B: Solid-State Materials for Advanced Technology*. Volume 177(12), pp. 949–955

Stoner, E.C., Wohlfarth, E.P., 1948. A Mechanism of Magnetic Hysteresis in Heterogeneous Alloy. *Philosophical Transactions of The Royal Society A*, Volume 240(826), pp. 599–642

Yustanti, E., Hafizah, M.A.E., Manaf, A., 2016. Exploring the Effect of Particle Concentration and Irradiation Time in the Synthesis of Barium Strontium Titanate (BST) $Ba_{(1-X)}Sr_XTiO_3$ (X:0-1) Nanoparticles by High Power Ultrasonic Irradiation. *International Journal of Technology*, Volume 7(6), pp. 1016–1025

Yustanti, E., Hafizah, M.A.E., Manaf, A., 2017. Surfactant-Assisted Synthesis of $Ba_{0.7}Sr_{0.3}TiO_3$ Nanoparticles by Mechanical Alloying and Ultrasonic Irradiation. *In:* International Conference on Engineering, Science and Nanotechnology 2016 (ICESNANO 2016), American Institute of Physics, Volume 1788, pp. 30119-1–4

Yustanti, E., Manaf, A., 2018. The Effect of Milling Time and Sintering Temperature on Mn, Ti Substituted Barium Hexaferrite Nanoparticle. *In:* Proceedings of the 3rd International Conference on Materials and Metallurgical Engineering and Technology (ICOMMET 2017) (ed. Hidayat, M. I. P.), American Institute of Physics, Volume 1945

Zhao, B., Fan, B., Shao, G., Zhao, W., Zhang, R., 2015a. Facile Synthesis of Novel Heterostructure Based on SnO_2 Nanorods Grown on Submicron Ni Walnut with Tunable Electromagnetic Wave Absorption Capabilities, *ACS Applied Materials & Interfaces*, Volume 7, pp. 18815–18823

Zhao, B., Fan, B., Xu, Y., Shao, G., Wang, X., Zhao, W., Zhang, R., 2015b. Preparation of Honeycomb SnO_2 Foams and Configuration-Dependent Microwave Absorption Features. *ACS Applied Materials & Interfaces*, Volume 7, pp. 26217–26225

Zhao, B., Guo, X., Zhao, W., Deng, J., Fan, B., Shao, G., Bai, Z., Zhang, R., 2017. Facile Synthesis of Yolk–shell Ni@void@SnO_2 (Ni_3Sn_2) Ternary Composites via Galvanic Replacement/Kirkendall Effect and Their Enhanced Microwave Absorption Properties. *Nano Research*, Volume 10, pp. 331–343

Zhao, B., Shao, G., Fan, B., Zhao, W., Zhang, R., 2015c. Investigation on the Electromagnetic Absorption Properties of Ni@TiO_2 and Ni@SiO_2 Composite Microspheres with Core-Shell Structure. *Physical Chemistry Chemical Physics*, Volume 17(4), pp. 2531–2539

Zhao, B., Zhao, W., Shao, G., Fan, B., Zhang, R., 2015d. Corrosive Synthesis and Enhanced Electromagnetic Absorption Properties of Hollow Porous Ni/SnO_2 Hybrids. *Dalton Transaction*, Volume 44(36), pp. 15984–15993

Zhao, B., Zhao, W., Shao, G., Fan, B., Zhang, R., 2015e. Morphology-Control Synthesis of a Core –Shell Structured NiCu Alloy with Tunable Electromagnetic-Wave Absorption Capabilities. *ACS Applied Materials & Interfaces*, Volume 7, pp. 12951–12960